Evaluation of Transition Performance to Jupiter Orbit Using Electrodynamic Tether System

Please select category below:
Normal Paper ■
Student Paper □
Young Engineer Paper □

Title

Hirohisa Kojima [1], and Pavel M. Trivailo [2]

[1] *Department of Aeronautics and Astronautics, Graduate School of Systems Design, Tokyo Metropolitan University, 6-6 Asahigaoka, Hino, Tokyo 191-0065, Japan*
[2] *School of Engineering, RMIT University, GPO Box 2476, Melbourne, Victoria 3001, Australia*

Abstract

An electrodynamic tether (EDT) system is expected as a propeller that generates acceleration and deceleration Lorentz forces with little propellant due to the generated current while generating electricity. Since the magnetic field intensity of Jupiter is approximately 14 times that of Earth and plasma is supplied from the satellite Io, the operation of an EDT system around Jupiter is attractive. Due to the influence of the surrounding plasma, the EDT system can only decelerate within the geostationary orbit called the drag arc. In the case of Jupiter, the drag arc is within approximately 2.24 times Jupiter's radius. Since the thrust of the tether greatly depends on the attitude of the EDT, stabilization of the attitude is essential in operation of an EDT as a thruster. In the present paper, we propose an attitude stabilization method to more efficiently decelerate a spacecraft around Jupiter and analyze the deceleration performance in a Jovian elliptical orbit.

Keywords: Electrodynamic Tether, Orbit Transfer, Drag Arc, Attitude Control, Flexible Tether

Introduction

Research and development has been conducted on the propulsion machine required for missions in outer space, and systems other than chemical and electric propulsion systems have been studied for practical use. Among these systems, there are systems connected by conductive string or tape with a length ranging from several kilometers to 100 kilometers, called an electrodynamic tether (EDT) [1]. This propulsion system uses the Lorentz force generated by interaction between the current on the tether and the magnetic field of the planet. The EDT generates an induced electromotive force on the entire EDT system including the spacecraft and tether by crossing the magnetic field of the central planet. This induced electromotive force causes a current to flow in the EDT, which generates a Lorentz force. Therefore, EDTs are attracting attention as highly efficient propulsion systems that require almost no propellant and enable power generation. The EDT thrust depends on the flight speed and the magnitude of the magnetic field. When the EDT system traverses the magnetic field, the thrust generally acts in the deceleration direction and enables power generation, but thrust can be generated in the acceleration direction by intentionally flowing an electric

current so as to cancel the induced electromotive force.

Since the plasma circulates in the direction of rotation of the central planet, the actual electromotive force induced by the EDT is the difference between the electromotive force induced by the plasma and the electromotive force induced by the EDT. The electric circuit is formed by collecting electrons from and releasing electrons to a plasma environment surrounding the EDT. Therefore, the existence of plasma and a magnetic field with a certain density is required for operation of the EDT. Since the EDT can be operated if this condition is satisfied, the EDT is expected to act as a system for reduction of the orbital speed and power generation for a spacecraft heading for another planet with plasma and a magnetic field. In particular, operation around Jupiter, which has a magnetic field that is approximately 14 times stronger than that of Earth and a large supply of plasma from the satellite Io, is of interest and has been studied extensively [2-9].

Jovian satellites such as Galilean satellites are thought to be clues to elucidate unknown aspects of the origin of solar system development. However, since it is not easy to place a spacecraft into the Jovian satellite orbit using chemical propulsion due to mass constraints, fly-by observations have mainly been carried out, but sufficient long-time observation of these satellites by spacecraft has not been done yet. Because of the plasma and magnetic field of Jupiter, an EDT system can become an orbit change thruster around Jupiter. From this point of view, the literature [2-9] has proposed decelerating a spacecraft approaching Jupiter with a hyperbolic trajectory using the EDT system and injecting satellites into elliptical orbits, and, eventually, circular orbits around Jupiter to observe Galilean satellites and other objects at low orbits around Jupiter.

The EDT thrust can be generated in the deceleration direction when the speed of the spacecraft on orbit is faster than the speed of the plasma. Since the plasma around the planet can be regarded as circling at the rotation angular velocity of the central planet, the velocity of the plasma increases as the orbital radius increases. Therefore, deceleration depends on the orbital speed of the spacecraft, and the deceleration range is only inside the geostationary orbit. The arc of the deceleration range is called “drag arc”. In the case of Jupiter, the planet’s mass is huge, and its rotation cycle is approximately 10 hours. Its drag arc is within approximately 2.24 times the radius of Jupiter. Since the EDT thrust is small compared to that for chemical propulsion, spacecraft cannot be decelerated by EDT thrust during only one flight in the drag arc. Repeated deceleration is required at the time of passing the drag arc until reaching a circular orbit.

Since the current flows in the direction projecting the induced electromotive force on the tether, and the direction of the generated thrust force is the cross product direction of the current and the magnetic field, the thrust is a function of the attitude of the tether portion. However, the EDT system includes tether vibration and pendulum-like motion with respect to the direction to the central planet. For this reason, in order to efficiently decelerate the spacecraft by the EDT, it is necessary to maintain an appropriate attitude of the EDT with respect to the magnetic field. The main bulk of previous research on attitude control by EDT is to suppress pendulum-like oscillation using Lorentz force by current on/off switching [11-15].

These studies assumed operation in a low circular orbit, and the center of mass of the system approximately corresponds to the position of the mother satellite. For this reason, suppression of pendulum-like motion was proposed to prevent the attitude from becoming unstable in the operation of the EDT, and the change in the attitude angle was assumed to be small. However, orbit transition is an operation with a high-eccentricity orbit, the attitude motion of the EDT system on a high-eccentricity orbit becomes complicated, and the variation of the attitude

angle becomes larger than that in the low orbit. For this reason, it is necessary to distribute sufficient mass to the daughter satellite, which also prevents unstable attitude motion of the system that could result in unstable rotation.

Although a conventional suppression method was assumed to be applicable on the whole orbit in past studies, simultaneous execution of the orbital speed deceleration and attitude control is applicable only within the drag arc for the case of a Jovian orbit. Therefore, appropriate attitude control inside the drag arc must be developed. This is the objective of the present study.

The dumbbell model, which assumes the tether to be a rigid rod, was widely used for attitude motion control in past studies on Jovian orbit missions. However, since the tether is flexible, the tether system could be operated in a high-eccentricity orbit, and the attitude of the EDT system is affected by the Lorentz force, its actual behavior must be different from that of the dumbbell model. The orbital motion limited (OML) theory [16-18] is a more realistic theory to describe the magnitude of the current that is collected from and released to the surrounding plasma on the tether surface.

The current increases in the range where the bias difference between the peripheral plasma and the tether is positive, and the current decreases in the range where this difference is negative. Therefore, although the distribution of the current/bias difference differs in the length direction, a more powerful current can be generated. As a result, in the present study, we propose a method by which to stabilize the attitude of a flexible EDT in the drag arc by analyzing the attitude motion using a model that incorporates the current distribution based on the OML theory and evaluate the deceleration performance to the Jovian orbit in detail.

System Model

In this section, we describe the orbital definition, the Jovian magnetic field model, the tether current model, the orbital motion, the attitude motion, and the flexible tether model.

Orbital Coordinate System

Figure 1 shows the definition of the coordinate system in the present study. We assume a geocentric inertial frame of Jupiter *OXYZ* with origin O at Jupiter's center. The *X*-axis of the frame is directed to the point of the vernal equinox, the *Z*-axis aligns with Jupiter's rotational axis, and the *Y*-axis is the direction orthogonal to both the *X*- and *Z*-axes based on the right-hand rule. The orbital coordinate system of the EDT has the center of Jupiter as the origin, the *x*-axis is in the orbital radial direction, and the *z*-axis is in the direction perpendicular to the orbit plane. The *y*-axis is the direction orthogonal to both the *x*- and *z*-axes based on the right-hand rule. The term $O\overline{xyz}$ is the ascending node and the orbital-plane-based coordinate frame, where the $\overline{x}$-axis is in the direction of the ascending node, $\overline{z}$-axis is in the direction perpendicular to the orbital plane, and the $\overline{y}$-axis is the direction orthogonal to both the $\overline{x}$- and $\overline{y}$-axes based on the right-hand rule. In the present study, the semi-major axis a, the eccentricity e, the longitude of the ascending node of the orbit Ω, the inclination i, the argument of perigee ϖ, and the true anomaly η are treated as the orbital elements.

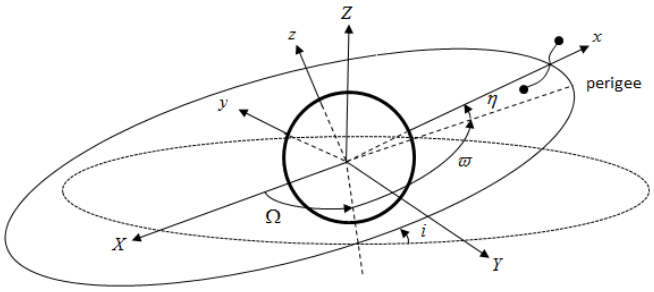

Fig. 1: Definition of the coordinate system

Magnetic Field Model of Jupiter

The general shape of the magnetic field of Jupiter is similar to that of Earth, but unlike Earth's magnetic field, the direction of the magnetic field is reversed. The Divine-Garrett model [19] determined Jupiter's magnetosphere, plasma sphere, and so on, based on data collected by Pioneer 10 and 11 and Voyager 1 and 2. In this model, the Jovian magnetic field can be regarded as a dipole model within approximately six times the Jupiter radius, and the inclination of the magnetic field with respect to the rotation axis is approximately 10.77°. Based on these considerations, the Jovian magnetic field used in the present study is a dipole model without an offset and is tilted by 10.77° with respect to the axis of rotation, as shown in Fig. 2. Assuming that the magnetic field is tilted by δ = 10.77° from the rotation axis about the *X*-axis at time 0, the magnetic field $\boldsymbol{B}$ at the radius *R* in the inertial coordinate system at time *t* is expressed as

$$\boldsymbol{B} = C_3(-\Omega_J t)C_1(-\delta)\frac{\mu_m}{R^3}\left(2\cos\theta\hat{r} + \sin\theta\hat{\theta}\right) \tag{1}$$

where $C_1(\bullet)$ and $C_3(\bullet)$ are the direct cosine matrix for rotation about the *x*- and *z*-axes, respectively, θ is the angle from the magnetic north pole to the orbital radius direction $\hat{r}$, and $\hat{\theta}$ is the direction on the plane of the orbital radius direction and the magnetic north pole and is perpendicular to the orbit radius direction.

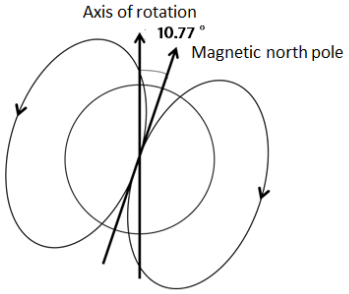

Fig. 2: Magnetic field model of Jupiter

Electric Current Model for Tether

An induced electromotive force is generated in an EDT system that crosses inside of a magnetic field at high speed. Since the induced electromotive force is generated by the motion of the plasma around Jupiter, the induced electromotive force $\boldsymbol{E}_m$ generated in the tether is calculated using the flight velocity of the EDT system $\boldsymbol{v}$, the plasma velocity $\mathbf{v}_{pl}$, and the magnetic field $\boldsymbol{B}$, as follows:

$$\boldsymbol{E}_m = (\boldsymbol{v} - \boldsymbol{v}_{pl}) \times \boldsymbol{B} \tag{2}$$

where the plasma velocity $\boldsymbol{v}_{pl}$, which can be regarded as being in a circular orbit at the angular velocity of Jovian rotation Ω_J, is given by

$$\boldsymbol{v}_{pl} = \Omega_J \widehat{\boldsymbol{Z}} \times \boldsymbol{R} \tag{3}$$

Electrons are exchanged between the plasma surrounding the tether and the surface of the bare tether, and the magnitude of the current changes in the longitudinal direction of the tether. Figure 3 shows a schematic representation of electron exchange between plasma and the tether. The OML theory is used to calculate the magnitude of the current along the tether. In the present study, we assume the use of a bare tether. Figure 4 shows the electric current magnitude $I(s)$ and potential difference between the plasma and tether $\Phi(s)$ at a distance of s from point A.

Electron exchange between the tether and the plasma varies in regions AB and BC. As shown in Fig. 3, the tether receives electrons from the plasma in region AB, and electrons are emitted to the plasma in region BC. This is because the potential difference between the tether and the plasma becomes positive near point A, and electrons flow into the tether from the plasma. Then, as electrons are gradually collected from the plasma, the electrons move toward the C direction. As a result, the potential difference decreases accordingly, and there is a point B at which the potential difference becomes zero. Since electrons are emitted from the tether toward the plasma after the potential difference becomes negative, the current and the potential difference decrease upon approaching point C.

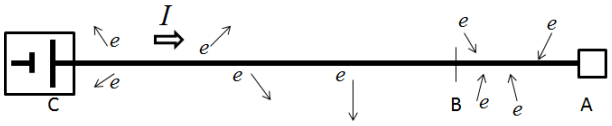

Fig. 3: Schematic representation of electron exchange between plasma and tether

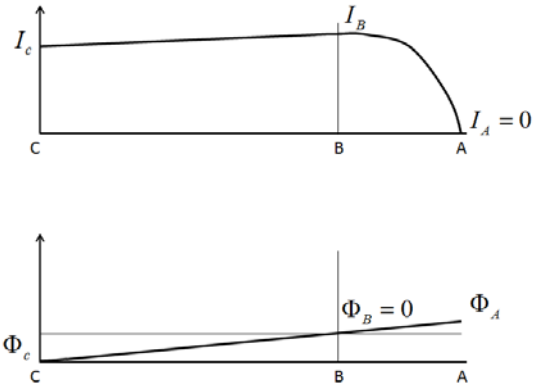

Fig. 4: Distributions of current magnitude I(s) and potential difference $\Phi(s)$

The current in the EDT is obtained from the OML theory. The current and the potential difference are a function of the plasma density around the EDT system and the induced electromotive force. Using the Divine-Garrett model [19] , the plasma density around Jupiter N_e (1/cm^3) within the region of the orbital radius $R_J < R < 3.8R_J$ is modeled as

$$N_e = 4.65\exp\left(\frac{7.68R_J}{R} - \left(\frac{R}{R_J} - 1\right)^2 \left(\lambda - \lambda_c\right)^2\right) \tag{4}$$

where $\lambda_c = (\tan\alpha)\cos(l - l_0)$, $l_0 = 21$ deg, $\alpha = 21$ deg, λ is the latitude, and l is the longitude of the EDT system. Although the plasma density varies along the tether, for simplicity, we assume herein that the plasma density is constant because the tether length is not so long, compared to the orbital radius.

As shown in Fig. 4, positive and negative regions occur in the potential difference between the tether and the plasma. Since the exchange of electrons is different in each region, the formula for obtaining the distribution of the current and the potential difference based on the

OML theory is also different in each region. Let the positive potential region be an anodic segment and let the negative potential region be a cathodic segment. Let $\Phi(s)$ be the potential difference at point s, let $I(s)$ be the current, and let $E_m(s)$ be a scalar quantity of the induced electromotive force along the tether at point s.

Anodic region AB: $\Phi(s) > 0$

$$\frac{dI(s)}{ds} = \frac{2(w_t + h_t)e_e N_e}{\pi}\sqrt{\frac{2e_e\Phi(s)}{M_e}} \tag{5}$$

$$\frac{d\Phi(s)}{ds} = \frac{I(s)}{\sigma_c w_t h_t} - E_m(s) \tag{6}$$

with boundary conditions $I(0) = 0, \Phi(0) = \Phi_A I(s_B) = I_B, \Phi(s_B) = 0$

Cathodic region BC: ($\Phi(s) < 0$)

$$\frac{dI(s)}{ds} = -\frac{2\mu(w_t + h_t)e_e N_e}{\pi}\sqrt{\frac{2e_e\,|\Phi(s)|}{M_e}} \tag{7}$$

$$\frac{d\Phi(s)}{ds} = \frac{I(s)}{\sigma_c w_t h_t} - E_m(s) \tag{8}$$

with boundary conditions $I(s_B) = I_B, \Phi(s_B) = 0, I(L_t) = I_C, \Phi(L_t) = \Phi_C$, where μ is a constant given by the mass of an electron M_e and the average mass of the surrounding ions M_i as

$$\mu = \sqrt{\frac{M_e}{M_i}} \tag{9}$$

Since $M_i \gg M_e$, the decreasing rate of current in the cathodic region is much smaller than the increasing rate of current in the anodic region. In addition, the following boundary condition is also given

$$V_{CC} + Z_T I_C = E_t(L_t - s_B) - \int_{s_B}^{L_t}\frac{I(s)}{\rho_c w_t h_t}ds \tag{10}$$

where E_t is the average induced electromotive force given by

$$E_t = \frac{1}{L_t}\int_0^{L_t} E(s)ds \tag{11}$$

The distributions of the current and the potential difference in the tether are obtained using Eqs. (5) through (8). However, because the initial value Φ_A needed for calculation of the distribution is unknown, it is necessary to determine its value. Considering the length variable s as a function of variable υ, the potential difference, the current, and the length for the anodic and cathodic regions are represented, respectively, as [21]

Anodic

$$\Phi(I) = \left(\frac{M_e^{\frac{1}{3}}}{2^{\frac{7}{3}}e_e}\left(\frac{3\pi}{\sigma_c N_e h_t}\right)^{\frac{2}{3}}\left(\frac{1}{w_t}\right)^{\frac{4}{3}}\right)(I_B - I)^{\frac{2}{3}}\left(2\sigma_c E_m(s(\upsilon))w_t h_t - I_B - I\right)^{\frac{2}{3}} \tag{12}$$

$$I(\upsilon) = \sigma_c E_m(s(\upsilon))w_t h_t - (\sigma_c E_m(s(\upsilon))w_t h_t - I_B)\cosh(\upsilon) \tag{13}$$

$$s(\upsilon) = \frac{4}{3}\left(\frac{\left(\frac{M_e}{\sigma_c w_t h_t}\right)^{\frac{1}{3}}}{2^{\frac{7}{3}}e_e}\left(\frac{3\pi}{N_e}\right)^{\frac{2}{3}}\right)(\sigma_c E_t w_t h_t - I_B)^{\frac{1}{3}}\left[f(\upsilon_0) - f(\upsilon)\right] \tag{14}$$

where $\upsilon \in [0, \upsilon_0]$ and

$$\upsilon_0 = \cosh^{-1}\left(\frac{\sigma_c E_t w_t h_t}{\sigma_c E_t w_t - I_B}\right) \tag{15}$$

$$f(\upsilon) = \int_0^{\upsilon} \sinh^{\frac{1}{3}}(x)dx \tag{16}$$

Cathodic

$$\Phi(I) = -\frac{1}{\mu^{\frac{2}{3}}}\left(\frac{M_e^{\frac{1}{3}}}{2^{\frac{7}{3}} e_e}\left(\frac{3\pi}{\sigma_c N_e h_t}\right)^{\frac{2}{3}}\left(\frac{1}{w_t}\right)^{\frac{4}{3}}\right)(I_B - I)^{\frac{2}{3}}\left(2\sigma_c E_m(s(\upsilon))w_t h_t - I_B - I\right)^{\frac{2}{3}} \tag{17}$$

$$I(\upsilon) = \sigma_c E_m(s(\upsilon))w_t h_t - (\sigma_c E_m(s(\upsilon))w_t h_t - I_B)\cosh(\upsilon) \tag{18}$$

$$s(\upsilon) = \frac{4}{3}\left(\frac{\left(\frac{M_e}{\sigma_c w_t h_t}\right)^{\frac{1}{3}}}{2^{\frac{7}{3}} e_e}\left(\frac{3\pi}{N_e}\right)^{\frac{2}{3}}\right)(\sigma_c E_t w_t h_t - I_B)^{\frac{1}{3}}\left[f(\upsilon_0) + \frac{f(\upsilon)}{\mu^{\frac{2}{3}}}\right] \tag{19}$$

where $\upsilon \in [0, \upsilon_T]$,

$$\upsilon_T = \cosh^{-1}\left(1 + \frac{I_B - I_C}{\sigma_c E_t w_t - I_B}\right) \tag{20}$$

$$s(\upsilon_T) = L_t \tag{21}$$

and the function f is the same as that for the anodic region. Using the above equations, the initial potential difference Φ_A is obtained as

$$\Phi_A = \left(\frac{M_e^{\frac{1}{3}}}{2^{\frac{7}{3}} e_e}\left(\frac{3\pi}{\sigma_c N_e h_t}\right)^{\frac{2}{3}}\left(\frac{1}{w_t}\right)^{\frac{4}{3}}\right) I_B^{\frac{2}{3}}\left(2\sigma_c E_t w_t h_t - I_B\right)^{\frac{2}{3}} \tag{22}$$

In order to determine the value of Φ_A from the above equation, it is necessary to determine the current I_B. Assuming that the total current decrease in the cathodic region is ϵ, $I_C = I_B - \epsilon$. Taking into account that the value of $s(\upsilon)$ is $s(\upsilon) = L_t$ at the boundary of the cathodic region $\upsilon = \nu_T$, and using I_B, ϵ and Eq. (9), we obtain the following two equations:

$$L_t - \frac{4}{3}\left(\frac{\left(\frac{M_e}{\sigma_c w_t h_t}\right)^{\frac{1}{3}}}{2^{\frac{7}{3}} e_e}\left(\frac{3\pi}{N_e}\right)^{\frac{2}{3}}\right)(\sigma_c E_t w_t h_t - I_B)^{\frac{1}{3}}\left[f(\upsilon_0) + \frac{f(\upsilon_T)}{\mu^{\frac{2}{3}}}\right] = 0 \tag{23}$$

$$Z_T(I_B - \epsilon) + V_{CC} + \frac{1}{\mu^{\frac{2}{3}}}\left(\frac{M_e^{\frac{1}{3}}}{2^{\frac{7}{3}} e_e}\left(\frac{3\pi}{\sigma_c N_e h_t}\right)^{\frac{2}{3}}\left(\frac{1}{w_t}\right)^{\frac{4}{3}}\right)\epsilon^{\frac{2}{3}}\left(2\sigma_c E_t w_t h_t - 2I_B + \epsilon\right)^{\frac{2}{3}} = 0 \tag{24}$$

Using the above two equations, ϵ and I_B can be determined. By substituting the determined values of ϵ and I_B into Eq. (22), the boundary value for determining the current in the tether is obtained. Finally, substituting these values into Eqs. (5) through (8), the current and potential difference along the tether can be determined.

Tether Modeling and Equations of Motion

In the present study, the tether is modeled as a multi-rod system, as shown in Fig. 5. The

mother satellite is labeled as 0, and the subsatellite is labeled as n. The mother satellite, subsatellite, and tether have masses of m_0, m_n, and m_t, respectively. The tether is divided into n rods, and the tether mass is distributed to rotatable joints between rods to represent the flexibility of the tether. Each rod is treated as a massless bar, and the length of the i-th rod is represented as ℓ_i. The in-plane and out-of-plane angles of the i-th rod in the orbital frame are represented as θ_i and ϕ_i, respectively.

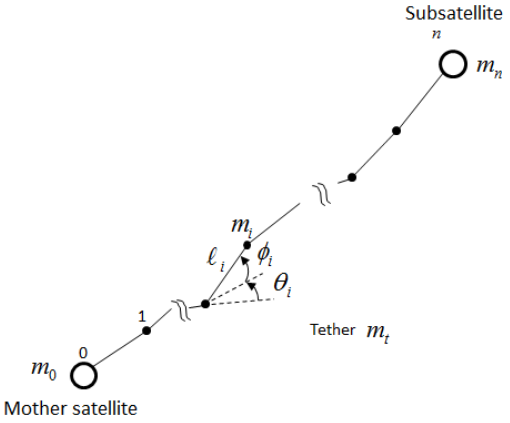

Fig. 5: Tether model

In the present study, the position of the center of mass of the system and the positions of the mother satellite and the i-th node relative to the center of mass of the system in the inertial frame are denoted as $\boldsymbol{R}$, $\boldsymbol{r}_0$, and $\boldsymbol{r}_i$, respectively. In this case, the positions of the mother satellite and the i-th node in the inertial frame are represented, respectively, as:

$$\boldsymbol{R}_0 = \boldsymbol{R} + \boldsymbol{r}_0 = \boldsymbol{R} + C^T \underline{\boldsymbol{r}}_0 \tag{25}$$

$$\boldsymbol{R}_i = \boldsymbol{R} + \boldsymbol{r}_i = \boldsymbol{R} + \boldsymbol{r}_0 + \boldsymbol{d}_i = \boldsymbol{R} + C^T (\underline{\boldsymbol{r}}_0 + \underline{\boldsymbol{d}}_i) \tag{26}$$

where $\underline{\boldsymbol{d}}_i$ is the position vector of the i-th node relative to the mother satellite in the orbital frame given by

$$\underline{\boldsymbol{d}}_i = \sum_{k=1}^{i} \underline{\ell}_k = \sum_{k=1}^{i} \begin{bmatrix} \ell_k \cos\theta_k \cos\phi_k \\ \ell_k \sin\theta_k \cos\phi_k \\ \ell_k \sin\phi_k \end{bmatrix} \tag{27}$$

and C^T is the transformation matrix from the orbital frame to the inertial frame. The velocity vector of the i-th node is given by

$$\boldsymbol{v}_i = \dot{\boldsymbol{R}} + \dot{\boldsymbol{r}}_i = \dot{\boldsymbol{R}} + C^T \underline{\dot{\boldsymbol{r}}} + \boldsymbol{\omega} \times C^T \underline{\boldsymbol{r}} \tag{28}$$

where $\boldsymbol{\omega}$ is the orbital angular velocity of the system. Since the center of mass of the system and its velocity must be coincident with $\boldsymbol{R}$ and $\dot{\boldsymbol{R}}$, respectively, the position of the mother satellite and its velocity relative to the center of mass of the system, $\boldsymbol{r}_0$ and $\dot{\boldsymbol{r}}_0$, must satisfy

$$\underline{\boldsymbol{r}}_0 = -\frac{1}{m_{sc}} \sum_{i=1}^{n} m_i \underline{\boldsymbol{d}}_i = -\frac{1}{m_{sc}} \sum_{i=1}^{n} m_i \sum_{k=1}^{i} \underline{\ell}_k \tag{29}$$

$$\underline{\dot{\boldsymbol{r}}}_0 = -\frac{1}{m_{sc}} \sum_{i=1}^{n} m_i \underline{\dot{\boldsymbol{d}}}_i = -\frac{1}{m_{sc}} \sum_{i=1}^{n} m_i \sum_{k=1}^{i} (\underline{\ell}_{k,\theta_k} \dot{\theta}_k + \underline{\ell}_{k,\phi_k} \dot{\phi}_k) \tag{30}$$

where

$$\underline{\ell}_{k,\theta_k} = \ell_k \begin{bmatrix} -\sin\theta_k \cos\phi_k \\ \cos\theta_k \cos\phi_k \\ 0 \end{bmatrix} \tag{31}$$

$$\underline{\ell}_{k,\phi_k} = \ell_k \begin{bmatrix} -\cos\theta_k \sin\phi_k \\ -\sin\theta_k \sin\phi_k \\ \cos\phi_k \end{bmatrix} \tag{32}$$

The acceleration vector of the i-th node in the inertial frame is given by

$$\boldsymbol{a}_i = \ddot{\boldsymbol{R}} + \ddot{\boldsymbol{r}}_i = \ddot{\boldsymbol{R}} + C^T \ddot{\underline{\boldsymbol{r}}}_i + \dot{\boldsymbol{\omega}} \times C^T \underline{\boldsymbol{r}}_i + 2\boldsymbol{\omega} \times C^T \dot{\underline{\boldsymbol{r}}}_i + \boldsymbol{\omega} \times (\boldsymbol{\omega} \times C^T \underline{\boldsymbol{r}}_i) \tag{33}$$

where the orbital angular velocity vector and orbital angular acceleration vector of the center of mass of the system in the inertial frame, $\boldsymbol{\omega}$ and $\dot{\boldsymbol{\omega}}$, are, respectively, given by

$$\boldsymbol{\omega} = \frac{1}{R^2}(\boldsymbol{R} \times \dot{\boldsymbol{R}}) \tag{34}$$

$$\dot{\boldsymbol{\omega}} = \frac{1}{R^2}(\boldsymbol{R} \times \ddot{\boldsymbol{R}}) - \frac{2}{R^4}(\boldsymbol{R} \times \dot{\boldsymbol{R}})(\boldsymbol{R} \cdot \dot{\boldsymbol{R}}) \tag{35}$$

The equation of motion of the i-th node is given by

$$m_i \boldsymbol{a}_i = \boldsymbol{F}_i^{(g)} + \boldsymbol{F}_i^{(ed)} + \boldsymbol{F}_i^{(t)} (= \boldsymbol{F}_i) \tag{36}$$

where $\boldsymbol{F}_i^{(g)}$, $\boldsymbol{F}_i^{(ed)}$, and $\boldsymbol{F}_i^{(t)}$ are the gravitational force, Lorentz force, and tether tension, respectively, acting on the i-th node. Although it is desirable to consider Jupiter's oblateness effect, the effect is not considered for simplicity in the present study, and only the electrodynamic force is treated as the perturbative acceleration source. In this case, the gravitational force acting on the i-th node can be represented as

$$\boldsymbol{F}_i^{(g)} = -\frac{m_i \mu_J \boldsymbol{R}_i}{R_i^3} \tag{37}$$

The Lorentz force acting on the i-th rod is given by

$$\boldsymbol{F}_i^{(L)} = \int_{s_{i-1}}^{s_i} \boldsymbol{I}(s) \times \boldsymbol{B}(s) ds \tag{38}$$

where s is the position vector along the tether, and s_i is the tether length at the i-th node from the mother satellite given by

$$s_i = \sum_{k=1}^{i} \ell_k \tag{39}$$

For simplicity, we assume that the electric current and the magnetic field vector on the i-th tether rod are constant and are represented by the values at the midpoint of the i-th tether rod. In this case, the Lorentz force acting on the i-th rod is given by

$$\boldsymbol{F}_i^{(L)} = \ell_i \, \boldsymbol{I}(\tilde{s}_i) \times \boldsymbol{B}(\tilde{\boldsymbol{s}}_i) \tag{40}$$

where $\tilde{\boldsymbol{s}}_i$ is the midpoint of the i-th tether rod. Furthermore, the above Lorentz force is equally distributed to nodes at both ends connecting the rod as

$$\boldsymbol{F}_i^{(ed)} = \begin{cases} \frac{1}{2}\boldsymbol{F}_1^{(L)} & \text{for } i = 0 \\ \frac{1}{2}(\boldsymbol{F}_i^{(L)} + \boldsymbol{F}_{i+1}^{(L)}) & \text{for } 0 < i < n \\ \frac{1}{2}\boldsymbol{F}_n^{(L)} & \text{for } i = n \end{cases} \tag{41}$$

Since the tether tension is an inner force, if all the rods representing tether are assumed to be inextensible, none of the rods absorb or emit energy by being extended or compressed. Therefore, when equations of motion are derived under this assumption, it is unnecessary to consider tether tension.

We derive equations of motion based on Kane's method. Using this approach, partial velocities must be derived. They are

$$\boldsymbol{v}_{i,1} = \frac{\partial \boldsymbol{v}_i}{\partial \dot{R}_x} = \widehat{\boldsymbol{X}} - \frac{1}{R^2}(\boldsymbol{r}_i \times [R^{\times}]_1) \tag{42}$$

$$\boldsymbol{v}_{i,2} = \frac{\partial \boldsymbol{v}_i}{\partial \dot{R}_y} = \widehat{\boldsymbol{Y}} - \frac{1}{R^2}(\boldsymbol{r}_i \times [R^{\times}]_2) \tag{43}$$

$$\boldsymbol{v}_{i,3} = \frac{\partial \boldsymbol{v}_i}{\partial \dot{R}_z} = \widehat{\boldsymbol{Z}} - \frac{1}{R^2}(\boldsymbol{r}_i \times [R^{\times}]_3) \tag{44}$$

$$\boldsymbol{v}_{i,2k+2} = \frac{\partial \boldsymbol{v}_i}{\partial \dot{\theta}_k} = \begin{cases} (1-\bar{\rho}_k)\underline{\ell}_{k,\theta_k} & ,1 \le k \le i \le n \\ -\bar{\rho}_k \underline{\ell}_{k,\theta_k} & ,0 \le i < k \le n \end{cases} \tag{45}$$

$$\boldsymbol{v}_{i,2k+3} = \frac{\partial \boldsymbol{v}_i}{\partial \dot{\phi}_k} = \begin{cases} (1-\bar{\rho}_k)\underline{\ell}_{k,\phi_k} & ,1 \le k \le i \le n \\ -\bar{\rho}_k \underline{\ell}_{k,\phi_k} & ,0 \le i < k \le n \end{cases} \tag{46}$$

Using Kane's equation

$$K_j^* + K_j = 0,\ j = 1, \cdots,\ 3+2n \tag{47}$$

$$K_j^* = \sum_{i=0}^{n} \boldsymbol{v}_{i,j} \cdot m_i(-\boldsymbol{a}_i) \tag{48}$$

$$K_j = \sum_{i=0}^{n} \boldsymbol{v}_{i,j} \cdot \boldsymbol{F}_i \tag{49}$$

the equations of motion can be obtained as

$$\boldsymbol{M}\ddot{\boldsymbol{x}} + \boldsymbol{f} = \boldsymbol{\tau} \tag{50}$$

where $\boldsymbol{M}$ is the mass matrix, $\boldsymbol{x}$ is the state vector, $\boldsymbol{x} = [R_x\ R_y\ R_z\ \theta_1\ \phi_1 \cdots \theta_n\ \phi_n]^T$, $\boldsymbol{f}$ is a nonlinear term vector, and $\boldsymbol{\tau}$ is a vector related to the gravity and the electrodynamic forces.

Orbital Elements

In papers that treated change in the orbital coordinate system due to the external forces, such as electrodynamic force, ordinary differential equations of six independent orbital elements, which are given in the form of Gaussian perturbation equations, were used. Instead of using Gaussian perturbation equations, in the present study, for simplicity and accuracy, the usual equations of motion in the rectangular coordinate system are used to calculate the motion of the EDT system. Six orbital elements are then calculated from the position and velocity vectors of the system.

The magnitude of the orbital angular velocity is given by

$$h = \left| \boldsymbol{R} \times \dot{\boldsymbol{R}} \right| \tag{51}$$

Using the orbital position and the velocity of the system, the semi major axis, inclination, and longitude of the ascending node of the orbit can be calculated, respectively, as

$$a = \frac{\mu_J}{\dfrac{2\mu_J}{R} - \dot{R}^2} \tag{52}$$

$$i = \cos^{-1}\left(\frac{R_x \dot{R}_y - R_y \dot{R}_x}{h} \right) \tag{53}$$

$$\Omega = \sin^{-1}\left(\frac{R_y \dot{R}_z - R_z \dot{R}_y}{\sqrt{h^2 - (R_x \dot{R}_y - R_y \dot{R}_x)^2}} \right) \tag{54}$$

The position and velocity vectors of the system in the ascending node and the orbital-plane-based coordinate frame are given by

$$\bar{R}_x = R_x \cos\Omega + R_y \sin\Omega \tag{55}$$

$$\bar{R}_y = (-R_x \sin\Omega + R_y \cos\Omega)\cos i + R_z \sin i \tag{56}$$

$$\dot{\bar{R}}_x = \dot{R}_x \cos\Omega + \dot{R}_y \sin\Omega \tag{57}$$

$$\dot{\bar{R}}_y = (-\dot{R}_x \sin\Omega + \dot{R}_y \cos\Omega)\cos i + \dot{R}_z \sin i \tag{58}$$

Using the above vectors, the argument of perigee, eccentricity, and true anomaly are obtained, respectively, as

$$\varpi = \text{atan2}\left(-\frac{-h\dot{\bar{R}}_x}{\mu_J} - \frac{\bar{R}_y}{R}, \frac{h\dot{\bar{R}}_y}{\mu_J} - \frac{\dot{\bar{R}}_x}{R} \right) \tag{59}$$

$$e = \sqrt{\left(\frac{h\dot{\bar{R}}_y}{\mu_J} - \frac{\dot{\bar{R}}_x}{R} \right)^2 + \left(-\frac{h\dot{\bar{R}}_x}{\mu_J} - \frac{\bar{R}_y}{R} \right)^2} \tag{60}$$

$$\eta = \text{atan2}(\bar{R}_y, \bar{R}_x) - \varpi \tag{61}$$

Consideration of the Decelerable Condition

Since the behavior of an EDT system on a high-eccentricity orbit becomes complicated, it is difficult for the EDT system to always have a stable attitude on the entire orbit. However, because the attitude change of the system in the drag arc is important for deceleration of the Jovian orbit, as shown in Fig. 6, it is necessary to consider the attitude within the drag arc that can decelerate the orbit.

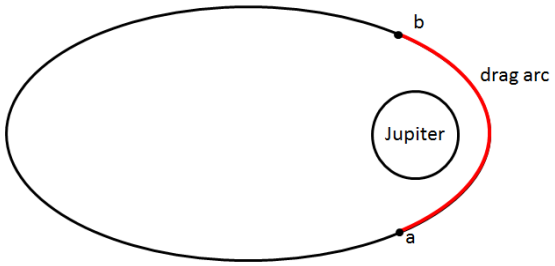

Fig. 6: Drag arc

Since the change of the orbital radius within the drag arc is limited, the influence of the difference in the orbital shape due to the eccentricity on the attitude variation within the drag arc is small compared to the attitude variation in the entire orbit. Therefore, a certain pattern appears in the attitude that can reduce the orbital speed. The influence of the difference in eccentricity on the attitude variation in the drag arc is represented by the transit time, velocity, and orbital shape. Since the EDT is required to generate the Lorentz force for deceleration and the Lorentz force is generated in the direction of the cross product of the velocity and magnetic field, it is desirable to maintain as far as possible the attitude of the tether that is perpendicular to the flight direction. However, due to the effect of orbital motion, the EDT system shows oscillation with some offset angle from the vertical. In addition, since the offset value changes on the orbit, it is difficult to maintain the attitude perpendicular to the flight direction. Therefore, for practical deceleration by the EDT, it is necessary to allow the attitude oscillation within some range, but not to tumble.

The thrust of the EDT is uniquely determined by the magnetic field and the flight speed, and a decelerating thrust can be generated only in the direction in which the attitude angular velocity increases. Therefore, even if the attitude angular velocity increases, it is necessary to maintain the attitude angle oscillation within the range that does not produce tumbling. The attitude oscillation in the drag arc depends on the state upon arriving at the drag arc: in-plane and out-of-plane angles and their velocities and eccentricities. By analyzing the dependency of the attitude motion in the drag arc on state variation at point a, it is possible to obtain the range of state required for the EDT system at point a. Hereafter, this required range of the state at point a is referred to as range A.

Due to nonlinear motion of the system on elliptic orbits, the state of the EDT system on elliptic orbits is not always within range A when arriving at point a. Therefore, we need to obtain the state at point b, which results in the state within range A when arriving at point a after orbital flight. Such a range of the state at point b is referred to as range B. By not only decelerating the orbital speed through the drag arc but also stabilizing the state within range B at point b, repeated stable deceleration can be achieved.

In the mission of an EDT system around Jupiter, the current flows from the high-altitude side to the low-altitude side of the system, as shown in Fig. 7. The current on the low-altitude side has a great effect on the position of the satellite, but the current on the high-altitude side does not. The attitude motion of each rod is represented by a set of four variables, i.e., in-plane/out-of-plane angles and their angular velocities, and the tether is represented by n rotational rods. Thus, 4n variables are used as the state for representing the tether shape and its motion in the present study. However, since the current distribution differs in the longitudinal direction according to the OML theory, it is impossible to obtain all of the states that can reduce the orbital speed and to directly control all of the nodes by current. In the present study, a straight line connecting the two satellites is virtually treated as a system attitude, and the in-plane and out-of-plane angles of this virtual line are represented as θ_t and ϕ_t, respectively. Their angular velocities are represented as $\dot{\theta}_t$ and $\dot{\phi}_t$, respectively, as shown in Fig. 8. Then, we numerically calculate the state of ranges A and B that can reduce the orbital speed.

In the present study, the transition from a hyper-elliptic orbit to a circular orbit is the target. Since the eccentricity of the trajectory having a perigee within the drag arc is $e = 0.23$ and a trajectory with an eccentricity of 1 is not an elliptic orbit, we consider the trajectory in the range of eccentricity of $0.23 \le e \le 0.98$. Hereinafter, the parameters listed in Table 1 are used in the present study.

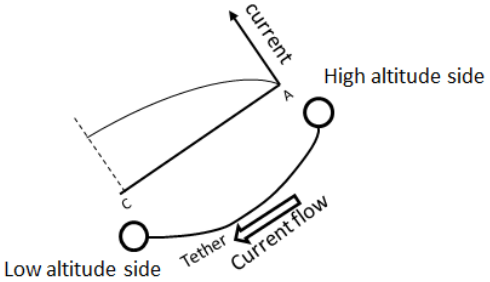

Fig. 7: Current flow

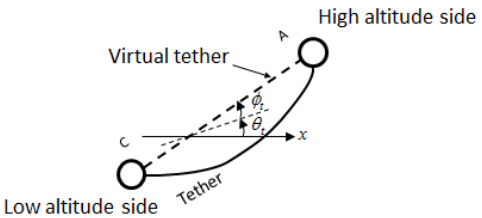

Fig. 8: Representative tether attitude

Table 1: Simulation parameters

Parameter	Value
tether length L_t	100 km
tether width w_t	3 cm
tether thickness h_t	0.05 mm
electrical conductivity σ_c	$3.767\times10^{7}\,\Omega^{-1}$
tether density ρ_t	$2.7\times10^{3}\,\mathrm{kg/m^3}$
tether mass m_t	405 kg
EDT mass M_{sc}	905 kg
tether material	Aluminum
resistance Z_t	$1,766.7\ \Omega$
cathodic contactor V_{cc}	30 V
electron e_e	1.602×10^{-19} ºC
electron mass M_e	9.109×10^{-31} kg
ion mass M_i	2.363×10^{-26} kg
Jupiter's radius R_J	71,492 km
gravity constant of Jupiter μ_J	$1.267\times10^{8}\,\mathrm{km^3/s^2}$
magnetic density at Jupiter's surface μ_m	4.225×10^{-4} T
number of rods n	5

State of range A

We determine the state of range A entering the drag arc by analyzing the attitude motion of the system for each state quantity. When the current does not flow on the tether, the out-of-plane angle and angular velocity become 0. Thus, the state of range A is obtained for three variables: in-plane angle, in-plane angular velocity, and eccentricity. Deceleration by Lorentz force does not suddenly change the attitude. The in-plane angle and angular velocity of the virtual rigid rod show anti-symmetric and symmetric shape, respectively, with respect to the true anomaly. Deceleration by Lorentz force has a tendency to reduce the angular velocity. In other words, the attitude tends to be stabilized by flowing the electric current. Therefore, the state of range A that can decelerate the system is obtained by calculating the unstable attitude motion for the case without a current and considering the state of the complementary set of unstable attitude motions.

Considering the deceleration in the drag arc, since the magnetic field becomes the largest in the vicinity of the perigee point, it is desirable to stabilize the attitude in the local vertical direction in the vicinity of the perigee point. We first choose the state such that $|\theta_t| < 0.2$ as the state of range A candidate. However, when deceleration is occurring, the attitude could not be stabilized in the local vertical direction in some cases, even within this range. Thus, it is necessary to exclude such states from the range. This occurs when the absolute value of the attitude angle after the perigee point becomes too large. In the present study, the state satisfying the condition $|\theta_{tp}| < |\theta_{t,max}| < |\theta_{t0}|$ is chosen as the state of range A, where θ_{tp} is the in-plane angle at the perigee point, $\theta_{t,max}$ is the maximum angle after passing the perigee point and until leaving the drag arc, and θ_{t0} is the in-plane angle upon entering the drag arc. Figure 9 shows the state of range A for eccentricities between 0.98 and 0.42 with an interval of 0.08.

Fig. 9: State of range A for eccentricities between 0.98 and 0.42 with an interval of 0.08

Among the parameters related to the drag arc, the flight time and the trajectory shape change in particular, depending on the eccentricity. When the flight time in the drag arc is prolonged, the motion in the drag arc becomes more sensitive to the initial value of the attitude parameter. Since the orbital angular velocity within the drag arc increases as the eccentricity increases, the amount of changes in the attitude angular velocity becomes larger at higher eccentricity. Therefore, the range of the initial value of the in-plane angular velocity also becomes wider for range A. As shown in Fig. 9, the state of range A formed

by the in-plane angle and angular velocity of the virtual rigid rod is wide in terms of both angle and angular velocity at high eccentricity. On the other hand, for low eccentricities, the flight time in the drag arc increases rapidly, and the range of angular velocity for range A decreases dramatically, as shown in Figs. 9(g) and 9(h).

State of range B

We choose the state at the departure from the drag arc as the state of range B such that the state fits into the state of range A obtained in the previous subsection when the system reenters the drag arc after departing from the drag arc. The state of range B is obtained by backward integrating the equations of motion of the EDT system from the state within range A. In this case, especially at high eccentricity, even if the system is stable within the drag arc, tumbling may occur due to prolongation of flight time outside the drag arc. Therefore, the range of the attitude angle of the virtual rigid rod is chosen as $-\pi \le \theta_t \le \pi$. Figure 10 shows the obtained state of range B for eccentricities between 0.98 and 0.42 with an interval of 0.08.

The transit time outside the drag arc becomes longer as the eccentricity becomes larger. For this reason, the attitude angle at point b changes greatly depending on slight changes in the state at point a. As mentioned above, the state of range B was obtained by backward integrating the equations of motion using finely divided values of the state of ranges obtained in the previous subsection. If the state at point a has continuous values for the in-plane angle and angular velocity, then the state at point b will be distributed within a range with some patterns. However, in orbits with an eccentricity of 0.74 or higher, the interval becomes so wide that a partial dense distribution of the state can be seen from Figs. 10(a) through 10(e), but general patterns were not found. In particular, in an orbit with an eccentricity of 0.90 or higher, the state at point b, which was obtained by backward integration, is only the state entering range A, tumbling, and orbiting outside of the drag arc.

When the trajectory has an eccentricity of 0.82 or less, even after orbiting outside the drag arc, the change in the state at point b corresponding to the change in the state at point a decreases. As shown in Figs. 10(f) to 10(g), the change is more noticeable when the state at point b is partially concentrated. In orbits with an eccentricity of 0.74 or higher, even if the state at point b is continuous, most of the states are a state of tumbling of the system during flight in the drag arc.

On the other hand, in orbits with an eccentricity of 0.58 or less, the state at point b corresponding to the state within range A is a state that does not tumble outside the drag arc and can exist after decelerating within the drag arc. For this reason, the distribution of the state of range B for an eccentricity of 0.58 or less is also concentrated into a narrow range.

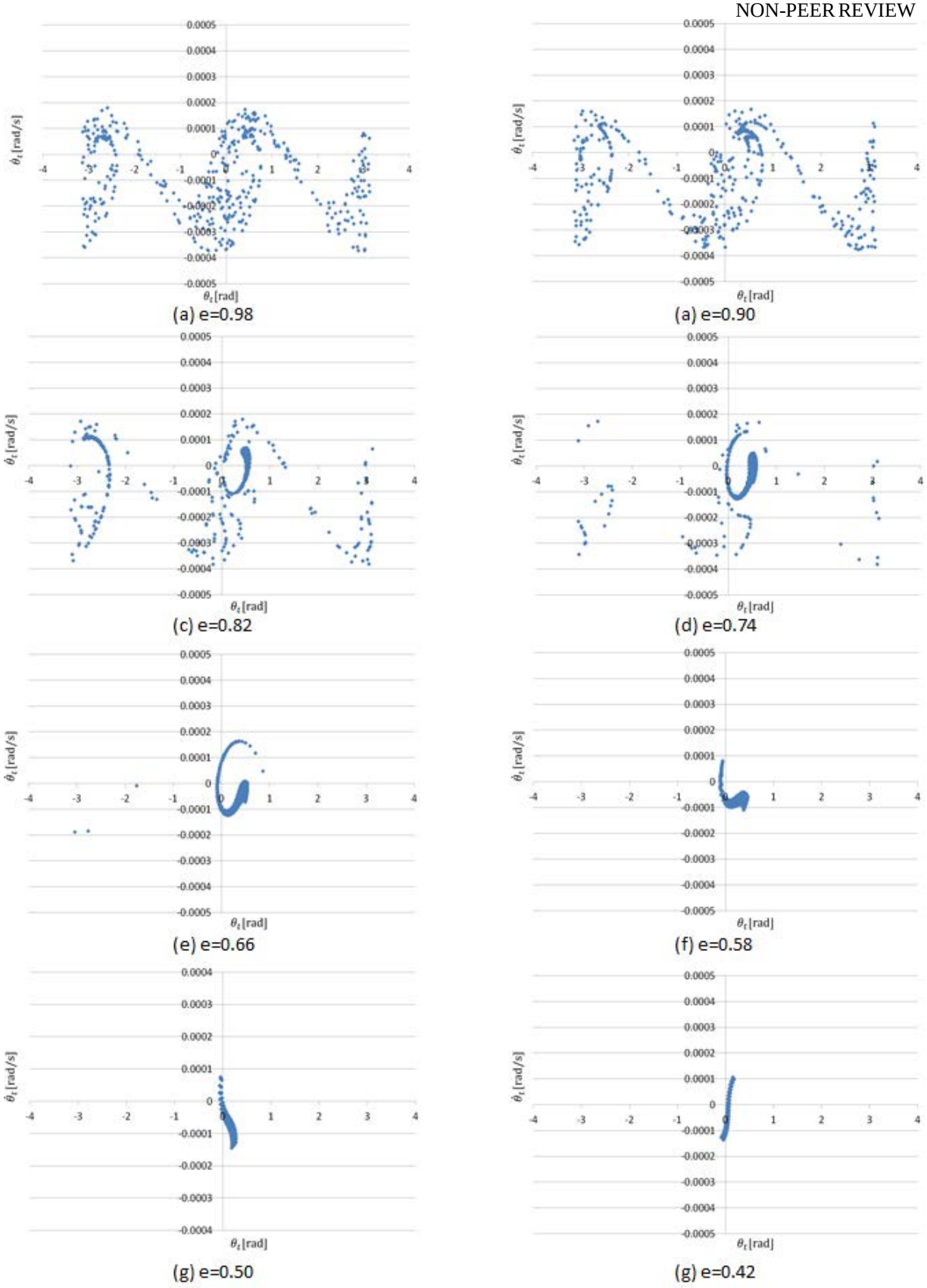

Fig. 10: State of range B for eccentricities between 0.98 and 0.42 with an interval of 0.08

Attitude Stabilization and Orbit Transient Strategy

In the previous section, the states of ranges A and B, in which deceleration can be achieved, were obtained as the necessary condition for circumferential deceleration. In this section, we describe a method to stably perform deceleration using these states of ranges. The deceleration

process is then obtained by simulation and the validity of the deceleration method is examined.

In a Jovian elliptical orbit, although the attitude motion becomes complicated with high eccentricity, it is possible to prevent tumbling in the drag arc due to the gravity gradient on the system. However, the attitude angle is affected by the Lorentz force. Therefore, it is necessary to change the state by setting the current to ON/OFF in order to stabilize the attitude and prevent destabilization of the attitude due to the continued current. The following are required for the EDT system during the drag arc.

1) Current ON/OFF control for attitude stabilization, and
2) Change from the state in range A to the state in range B.

The EDT system in the present study has five state variables: in-plane angle and angular velocity, out-of-plane angle and angular velocity, and eccentricity. Similarly, Ref. [11] determines ON/OFF current switching using the same state variables. Therefore, in the present study, the attitude stabilization method using ON/OFF current switching is considered by referring to Ref. [11].
A function by which to determine the ON/OFF setting of current V_e is given as follows:

$$V_e = 4 - 3\cos^2\phi_t \cos^2(\theta_t - \theta_p) + \frac{1}{\omega^2}\left\{\cos^2\phi_t((\dot{\theta}_t - \dot{\theta}_p)^2 - \omega^2) + \dot{\phi}_t^2\right\} \quad (62)$$

where θ_p and $\dot{\theta}_p$ are the in-plane angle and in-plane angular velocity, respectively, for the case in which the sum of the attitude kinetic and potential energy is minimum. Since the out-of-plane angle/angular velocity are both zero when the sum of the attitude kinetic and potential energy becomes minimum, using the moment of inertia of the virtual rigid body for the EDT system, I_x, I_y, and I_z, the minimum sum of the in-plane attitude kinetic and potential energies can be expressed as [21]

$$U_a = \frac{1}{2} I_z(\dot{\eta} + \dot{\theta}_t)^2 - \frac{\mu_J\left\{I_z + 3(I_x - I_y)\cos 2\theta_t\right\}}{4|R|^3} \quad (63)$$

We will find θ_p and $\dot{\theta}_p$ such that the sum of the in-plane attitude kinetic and potential energies becomes minimum. Since the attitude energy and the orbital energy are partially converted into each other, the sum of the in-plane attitude kinetic and potential energies is not constant. Thus, in order to evaluate the attitude energy, it is desirable to calculate its mean value as follows:

$$\bar{U}_e = \lim_{T\to\infty}\frac{1}{T}\int_0^T U_a dt \quad (64)$$

For calculating the above value, it is necessary to choose the calculation duration *T*. In the present study, by referring to [21], a duration of 500 orbits is chosen for *T*. Assuming that the periodic in-plane libration motion is approximated in the form of a function of the true anomaly and eccentricity as

$$\theta_p(\eta, e) = A_1(e)\sin\eta + A_2(e)\sin 2\eta \quad (65)$$

we obtained the coefficient amplitude of periodic in-plane libration motions, A_1 and A_2 for each eccentricity. Figure 11 shows the relationship between amplitudes A_1 and A_2 and eccentricities. As the result of approximation as a function of eccentricity, $A_1(e)$ and $A_2(e)$ are determined as follows:

$$A_1(e) = 0.39e$$
$$A_2(e) = 0.17e^3 - 0.21e^2 + 0.23e$$

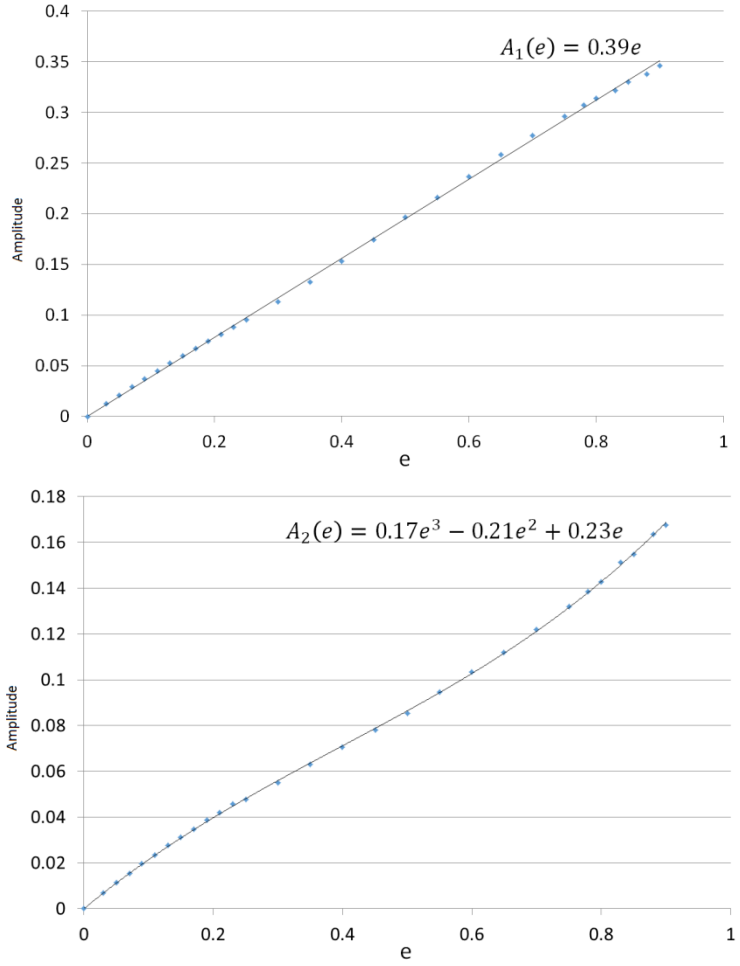

*Fig. 11: R*elationship between amplitude and eccentricity

The current is turned on as long as V_e resulting from these values does not exceed the threshold value V_{th} and when V_e exceeds the threshold, the current is turned off. In the present study, by referring to Ref. [11], the threshold V_{th} is set to 1.2 for the case of orbit $e \geq 0.23$ until all parts of the orbit enter the drag arc and 0.2 for the case of orbit $e < 0.23$.

We describe a method of changing the state quantity within range A to range B for deceleration. The deceleration process in the drag arc consists of two phases. The first phase is to decelerate to the target eccentricity rate, and then the ON/OFF switching of the current is conducted in order to change to the target state quantity. What is important at this time is a target state quantity existing within the state of range B. The selection of the target state depends on whether the attitude motion outside the drag arc is a tumbling motion. First, we explain the case of tumbling. The energy of the attitude motion $(\theta_b, \dot{\theta}_b)$ exceeds the threshold value. Therefore, the in-plane angle of the target state θ_b is the angle such that $\theta_b > \theta_a$, where θ_a is the angle at point a. Next, we explain the case without tumbling. Since the attitude motion is stabilized around the equilibrium point, the energy determined from the target state quantity decreases. Therefore, the target state quantity is chosen such that it is within the state of range B, and its energy is equal to or less than the attitude kinetic energy at point a. In accordance with this criterion, the ON/OFF switching control method should be chosen: (1) the tumbling case and (2) the non-tumbling case.

(1) Tumbling case

Motion estimation is performed to estimate the state at drag arc exit point b by assuming the continued current for a certain period of time from the drag arc entry point a and no current until the drag arc exit point b. When the difference in the state from the target value converges within

the tolerance $|\Delta\theta| < 10^{-4}$ and $|\Delta\dot{\theta}| < 10^{-6}$, the current is turned off.

(2) Non-tumbling case

Since the attitude motion outside the drag arc does not become a tumbling motion, in order to suppress the attitude motion, the current is turned on in the case that the angular velocity of the virtual rigid rod is $\dot{\theta} < 0$, and is turned off otherwise. Motion estimation is then performed in order to estimate the state at the drag arc exit point b under the assumption that the current is turned off until the drag arc exit point b. Similarly to the tumbling case, when the difference in the state from the target state converges within the tolerance $|\Delta\theta| < 10^{-4}$ and $|\Delta\dot{\theta}| < 10^{-6}$, the current is turned off until re-reaching the drag arc entry point a. As a result of this control strategy, the energy of the attitude motion decreases and orbital motion does not become a tumbling motion outside the drag arc.

Result of Numerical Simulation

In order to validate the control strategy described above, numerical simulation is carried out using the following initial conditions:

$$\eta = 4.994 \text{ [rad]},\ e = 1.02,\ \theta_i = -0.0231 \text{ [rad]},\ \dot{\theta}_i = 0.5527,\ \phi_i = \dot{\phi}_i = 0 \quad (i = 1, \ldots, 5)$$

Figure 12 shows the shape of trajectories and eccentricity changes obtained through the numerical simulation. After the system passed through the drag arc 13 times, all parts of the trajectory entered the drag arc, and the trajectory then became a circular orbit. A total of 91.21 days was required until convergence to a circular orbit. The eccentricity of 0.04 to 0.07 was reduced during one pass through the drag arc. As the trajectory in the drag arc became longer for lower orbits, the amount of eccentricity decrease during one pass became larger.

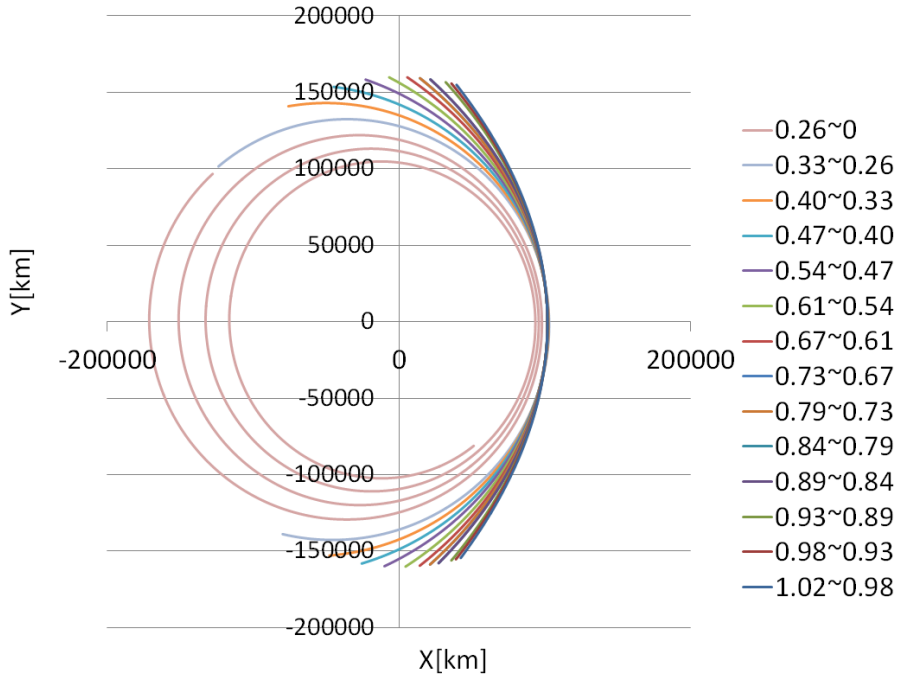

Fig. 12: Shape of trajectories and eccentricity changes

Conclusion

In the present study, we have proposed a method by which to reduce the velocity of a spacecraft headed toward Jupiter and to shift its elliptic orbit to a circular orbit using an EDT. Then, we investigated the validity of the proposed method by performing a motion analysis.

Since the range of the drag arc that can reduce the spacecraft velocity by the EDT is a part of the orbit, the motion of the EDT system at this drag arc entry point is particularly important when decelerating. Therefore, in the present study, the following method was adopted in order to decelerate in the orbit. First, the state of range A of the EDT system at the entry point of the drag arc was obtained when decelerating becomes possible within the drag arc. Next, the state of range B at the drag arc escape point is obtained so that the state quantity at the drag arc entry point can enter the state of range A after the spacecraft orbits outside the drag arc and reaches the drag arc entry point. We then have proposed a method that enables orbital deceleration and stable transition from the state within range A to that in range B while passing the drag arc. Numerical calculations confirmed that convergence from the hyperbolic trajectory to the circular orbit can be achieved by an EDT around Jupiter.

References

1. Sanmartin, J. R., Martinez-Sanchez, M., and Ahedo, E., ``Bare Wire Anodes for Electrodynamic Tethers," Journal of Propulsion and Power, Vol. 9, No. 3, 1993, pp. 353-360.

2. Charro, M., Sanmartin, J. R., Bombardelli, C., Sanchez-Torres, A., Lorenzini, E. C., Garrett, H. B., and Evans, R. W., ``A Proposed Two-Stage Two-Tether Scientific Mission at Jupiter," IEEE Transactions on Plasma Science, Vol.40, No.2, 2012, pp. 274-281.

3. Sanmartin, J. R., Charro, M., Lorenzini, E. C., Garrett, H. B., Bombardelli, C., and Bramanti, C., ``Electrodynamic Tether at Jupiter—I: Capture Operation and Constraints," IEEE Transactions on Plasma Science, Vol. 36, No.5, 2008, pp. 2450-2458.

4. Sanmartin, J. R., Charro, M., Lorenzini, E. C., Garrett, H. B., Bombardelli, C., and Bramanti, C., ``Electrodynamic Tether at Jupiter-:II: Fast Moon Tour After Capture," IEEE Transactions on Plasma Science, Vol.37, No.4, 2009, pp.620-626.

5. Sanmartin, J. R., Bombardelli, C., Charro, M., and Lorenzini, E., ``Electrodynamic Tether for Scientific Mission in Low Jovian Orbit," 7th International Energy Conference 2-5August 2009, Denver, Colorado, AIAA 2009-4549.

6. Sanmartin, J. R., Charro, M., Bramanti, C., and Bombardelli, C., ``Electrodynamic Tether Microsats at the Giant Planets," Ariadna Ariadna Study/05/3203, ESA.

7. Atchison, J. A., and Peck, M. A., ``Lorentz-Augmented Jovian Orbit Insertion," Journal of Guidance, Control, and Dynamics, Vol.32, No.2, 2009, pp. 418-423.

8. Pelaez, J., Bombardelli, C., and Scheeres, D. J., ``Dynamics of a Tethered Observatory at Jupiter," Journal of Guidance, Control, and Dynamics, Vol.35, No.1, 2012, pp.195-207.

9. Gallagher, D. L., Johnson, L., Moore, J., and Bagenal, F., ``Electrodynamic Tether Propulsion and Power Generation at Jupiter," NASA/TP—1998–208475.

10. Kashihara, K., Qu, D. et al., ``Ground Experiments and Computer Simulations of Interaction between Bare Tether and Plasma," IEEE Transactions on Plasma Science, 2008, pp.2324-2335.

11. Takeichi, N., ``Practical Operation for Deorbit of an Electrodynamic Tethered System," Journal of Spacecraft and Rockets, Vol. 43, No. 6, 2006, pp.1283-1288.

12. Zhong R., and Zhu, Z. H., ``Long-term Libration Dynamics and Stability Analysis of Electrodynamic Tether in Spacecraft Deorbit," Journal of Aerospace Engineering, Vol. 27, No. 5, 2012.

13. Zhong, R., and Zhu, Z. H., ``Optimal Current Switching Control of Electrodynamic Tethers for Fast Deorbit," Journal of Guidance, Control, and Dynamics, Vol. 37, No. 5, 2014, pp. 1501-1511.

14. Zhong, R., and Zhu, Z. H., ``Optimal Control of Nanosatellite Fast Deorbit Using Electrodynamic Tether," Journal of Guidance, Control, and Dynamics, Vol. 37, No.4, 2014, pp.1182-1194.

15. Li, G., Zhu, Z. H., and Meguid, S. A., ``Libration and Transverse Dynamic Stability

Control of Flexible Bare Tether Systems in Satellite Deorbit," Aerospace Science and Technology, Vol. 49, 2016, pp.112-129.

16. Sanmartín J., and Estes, R., ``The Orbital-Motion-Limited Regime of Cylindrical Langmuir Probes," Physics of Plasmas, Vol. 6, 1999, pp. 395–405.

17. Estes, R. D., and Sanmartin, J. R., ``Cylindrical Langmuir Probes Beyond the Orbital-Motion-Limited Regime," Physics of Plasmas, Vol. 7, No. 10, 2000, pp.4320-4325.

18. Chin, X., and Sanmartín, J., ``Low Work-Function Thermionic Emission and Orbital-Motion-Limited Ion Collection at Bare-Tether Cathodic Contact," Physics of Plasmas, Vol.22, 2015, 053504.

19. Divine, N., and Garrett, H. B., ``Charged Particle Distribution in Jupiter's Magnetosphere," Journal of Geophysical Research, Vol.88, No. A9, 1983, pp.6889-6903.

20. Sanjurujo, M., Scheeres, D. J., and Pelaez, J., ``Jovian Capture of a Spacecraft with Self-Balanced Electrodynamic Bare Tether," Journal of Spacecraft and Rockets, Vol. 51, No.5, 2014, pp. 1401-1412.

21. Sanjurujo, M., and Pelaez, J., ``Self Balanced Bare Electrodynamic Tethers Space Debris Mitigation and Other Applications," Departamento de Fisica Aplicada a la Ingenieria Aeronautica Esucula Tecnica Superior de Ingenieros Aeronauticos, 2009.

22. Takeichi, N., Natori, M. C., Okuizumi, N., and Higuchi, K., ``Coupled Librational and Orbital Motions of a Large-Scale Spacecraft," Transactions of the Japan Society for Aeronautical and Sciences, Vol. 46, No. 152, 2003, pp. 61-67.

23. Williams, P., ``Electrodynamic Tethers under Forced-Current Variations part2: Flexible-Tether Estimation and Control," Journal of Spacecraft and Rockets, Vol.47, No.2, 2010, pp.320-333.

24. Williams, P., ``Deployment/Retrieval Optimization for Flexible Tethered Satellite Systems," Nonlinear Dynamics, Vol.52, No.1-2, 2008, pp.159-179.

25. Zhong, R., and Zhu, Z. H., ``Libration Dynamics and Stability of Electrodynamic Tethers in Deorbit," Celestial Mechanics and Dynamical Astronomy, Vol. 116, No. 3, pp.279-298.

26. Fuhrhop, R. P., Choiniere, E., and Gilchrist, E., ``A Comparison of Laboratory Experimental and Collection Performance of Some Bare Tether Geometries," AIAA, Space 2009 Conference \& Exposition 14-17, 2009, Pasadena, California, AIAA 2009-6659.

27. Khan, S. B., Sunmartin, J. R., ``Analysis of Tape Tether Survival in LEO Against Orbital Debris," Advances in Space Research, Vol.53, No.9, 2014, pp.1370-1376.

28. Pardini, C., Hanada, T., and Krisko, P. H., ``Benfits snd Risks of Using Electrodynamic Tethers to De-Orbit Spacecraft," IAC-06-B6.2.10.

29. Ikeda, T., Nakamura, Y., Yamagiwa, Y., Otsu, H., Kawamoto, S., Ohkawa, Y., and Nakajima, A., ``Multiple Bare Tethers for Electrodynamic Tether Propulsion," the 30th International Electric Propulsion Conference, Florence, Italy, 17-20, 2007.

30. Khurana, K. K., ``Euler Potential Models of Jupiter's Magnetospheric Field," Journal of Geophysical Research, Vol.102, No.A6, 1997, pp.11295-11306.

31. Connerney, J. E. P., Acuna, M. H., Ness, N. F., and Satoh, T., ``New Models of Jupiter's Magnetic Field Constrained by the Io Flux Tube Footprint," Journal of Geophysical Research, Vol.103, No.A6, 1998, pp.11929-11939.

32. Beletsky, V. V., Levin, E. M., Translated by E. M. Levin, ``Dynamics of Space Tether System," Advances in The Astronautical Sciences, 1993.

33. Sanmartin, J. R., Lorenzini, E. C., and Martinez-Sanchez, M., ``Electrodynamic Tether Applications and Constraints," Journal of Spacecraft and Rockets, Vol.47, No.3, 2010, pp.442-456.

34. Jupiter Fact Sheet, http://nssdc.gsfc.nasa.gov/planetary/factsheet/jupiterfact.html,

35. Bombardelli, C., Lorenzini, E. C., Sanmartin, J. R., ``Jupiter Power Generation with Electrodynamic Tethers at Constant Orbital Energy," Journal of Propulsion and Power, Vol.25, No.2, 2009, pp.415-423.

36. Sanmartin, J. R., and Lorenzini, E. C., ``Exploration of Outer Planets Using Tether for Power and Propulsion," Journal of Propulsion and Power, Vol.21, No.3, 2005, pp.573-576.

37. Bombardelli, C., ``Power Density of a Bare Electrodynamic Tether Generator," Journal of Propulsion and Power, Vol.28, No.3, 2012, pp.664-668.

38. Sanmartin, J. R., ``A Review of Electrodynamic Tethers for Science Applications," Plasma Sources Science and Technology, Vol.19, No.3, 2010, pp.034022.

39. Curreli, D., Lorenzini, C., Bombardelli, C., Sanjurjo-Rivo, M., Pelaez, J., Scheeres, D., and Lar, M., ``Three-Body Dynamics and Self-Powering of an Electrodynamic Tether in a Plasmasphere," Journal of Propulsion and Power, Vol.26, No.3, 2010, pp.385-393.